

Two-Screen Scattering in CRAFT FRBs

Mawson W. Sammons,¹★ Adam T. Deller,² Marcin Glowacki,¹ Kelly Gourdjji,² C. W. James,¹
J. Xavier Prochaska,^{3,4,5} Hao Qiu,⁶ Danica R. Scott,¹ R. M. Shannon,² and C. M. Trott,¹

¹International Centre for Radio Astronomy Research, Curtin University, Bentley, WA 6102, Australia

²Centre for Astrophysics and Supercomputing, Swinburne University of Technology, Hawthorn, VIC, 3122 Australia

³Department of Astronomy and Astrophysics, University of California, Santa Cruz, CA 95064, USA

⁴Kavli Institute for the Physics and Mathematics of the Universe, 5-1-5 Kashiwanoha, Kashiwa 277-8583, Japan

⁵Division of Science, National Astronomical Observatory of Japan, 2-21-1 Osawa, Mitaka, Tokyo 181-8588, Japan

⁶SKA Observatory, Jodrell Bank, Macclesfield, SK11 9FT United Kingdom

Accepted XXX. Received YYY; in original form ZZZ

ABSTRACT

Temporal broadening is a commonly observed property of fast radio bursts (FRBs), associated with turbulent media which cause radiowave scattering. Similarly to dispersion, scattering is an important probe of the media along the line of sight to an FRB source, such as the circum-burst or circum-galactic mediums (CGM). Measurements of characteristic scattering times alone are insufficient to constrain the position of the dominant scattering media along the line of sight. However, where more than one scattering screen exists, Galactic scintillation can be leveraged to form strong constraints. We quantify the scattering and scintillation in 10 FRBs with 1) known host galaxies and redshifts and 2) captured voltage data enabling high-time resolution analysis. We find strong evidence for two screens in three cases. For FRBs 20190608B and 20210320C, we find evidence for scattering screens less than approximately 16.7 and 3000 kpc respectively, from their sources, consistent with the scattering occurring in the circum-burst environment, the host ISM (inter-stellar medium) or the CGM. For FRB 20201124A we find a low modulation index that evolves over the burst’s scattering tail, indicating the presence of a scattering screen ≈ 9 kpc from the host, and excluding the circum-burst environment from potential scattering sites. By assuming that pulse broadening is contributed by the host galaxy ISM or circum-burst environment, the lack of observed scintillation in four FRBs in our sample suggests that existing models may be poor estimators of scattering times associated with the Milky Way’s ISM, similar to the anomalously low scattering observed for FRB 20201124A.

Key words: fast radio bursts – scattering – intergalactic medium

1 INTRODUCTION

Fast radio bursts (FRBs) are short duration (μs – ms), extragalactic, radio frequency bursts (Lorimer et al. 2007; Thornton et al. 2013). In addition to intrinsic time-frequency structure, FRBs are dispersed and often contain the hallmarks of multi-path propagation, arising from propagation through a turbulent medium. While the intergalactic medium (IGM) is often responsible for a sizeable portion of FRB dispersion (Macquart et al. 2020), due to its tenuous density, it is not expected to contribute significantly to the scattering, with estimates typically as low as $\sim 10 \mu\text{s}$ at 1 GHz (Macquart & Koay 2013; Cordes et al. 2022). This conclusion is supported by the observed lack of correlation between FRB dispersion measures (DM) and scattering times (Chawla et al. 2022; Gupta et al. 2022).

Similarly, the Milky Way interstellar medium (ISM) is not expected to dominate the scattering observed in FRBs at high Galactic latitudes, with scattering times inferred from pulsars (Cordes & Lazio 2003) being $\lesssim 10 \mu\text{s}$ for lines of sight more than 30° away from the Galactic plane. Assuming that the host galaxies of FRBs are similar

to the Milky Way, the symmetry of the scattering process leads to the conclusion that, on average, host galaxy ISMs are also unlikely to be singularly responsible for the observed FRB scattering (Simha et al. 2020; Chawla et al. 2022).

Due to their large geometric leverage, intervening galaxies are a potential source of large scattering in FRBs. For a high redshift population ($z \sim 5$), intervening galaxies have been forecast to be the dominant source of scattering (Ocker et al. 2022a). For FRBs with $z \lesssim 1$, however, the probability of intersecting a foreground galaxy is insufficient for them to be the dominant source of scattering in the population (Macquart & Koay 2013; Prochaska & Neeleman 2018; Chawla et al. 2022; Ocker et al. 2022a).

A potentially important scattering region is within the circum-burst environment, which has long been suggested as the site of the \gtrsim ms scattering times and $\gtrsim 100 \text{ rad m}^2$ rotation measures (RMs) observed in some FRBs (Masui et al. 2015). Measurements of RM variability in some repeating FRBs have supported this scenario, with large variations over short durations requiring a dense, magnetised medium near the source (Michilli et al. 2018; Hilmarsson et al. 2021; Anna-Thomas et al. 2022). Recent measurements of scattering variability in FRB 20190520B provide the tightest limits yet, with variation

★ E-mail: mawson.sammons@postgrad.curtin.edu.au

on minute timescales requiring the dominant scattering media to be within at most 0.4 AU of the source, and potentially within $\sim 10^4$ km (Ocker et al. 2022a). In this scenario, scattering serves as an important probe of the circum-burst region which would inform our understanding of FRB progenitors, favouring formation channels where the central engine evolves in a dense turbulent magnetised medium, such as a magnetar embedded within a nebula (Margalit & Metzger 2018).

Another region of interest is the circum-galactic media (CGM) of foreground galaxies. To date, observations of FRBs passing through the CGM/halos of intervening galaxies have shown very little scattering, with only as much as $\sim 80 \mu\text{s}$ recorded at 1.4 GHz (Prochaska et al. 2019; Connor et al. 2020, 2023). The possible presence, however, of cloudlets of cold gas in the CGM, inferred from quasar absorption spectra (McCourt et al. 2018), has the potential to cause scattering consistent with that observed in the FRB population (Vedantham & Phinney 2019, see Prochaska et al. (2019) for a corrected description). If this model is correct, then FRBs could serve as an important probe of the CGM. As discussed by Vedantham & Phinney (2019), distinguishing between scattering in the CGM and circum-burst media will be crucial.

For scattering that is well approximated by a thin screen model, the degeneracy between the angular broadening and screen distance makes it difficult to directly constrain where the scattering is occurring based only on the pulse-broadening time. For repeating FRBs, a direct constraint can be made by observing the variation of decorrelation bandwidth (ν_{DC}) or temporal broadening over time (t_{scatt}) (Ocker et al. 2022a; Main et al. 2022). For FRBs that are not seen to repeat, a variability study cannot be conducted; however, in cases where scattering and scintillation have been contributed by separate screens, the scattering geometry can be constrained using the observation of only a single burst (Masui et al. 2015; Farah et al. 2018; Ocker et al. 2022b). This can allow not only for the distinction between host and intervening scattering screens, but also constrain the level of scatter-broadening in the Milky Way, for independent comparison with electron distribution models such as NE2001 and YMW16 (Cordes & Lazio 2003; Yang & Zhang 2017, respectively).

Where previously Day et al. (2020) relied on lower time resolutions and image-plane-based techniques, it is now routinely possible to conduct detailed burst morphology analysis, of the type undertaken by Cho et al. (2020), for all Commensal Real-time ASKAP (Australian Square Kilometre Array Pathfinder) Fast Transient survey (CRAFT) FRBs with the advent of the CELEBI post-processing pipeline (Scott et al. 2023). This allows for the high-precision estimates of ν_{DC} and t_{scatt} , required to robustly identify scintillation and scattering. We are therefore motivated to search for evidence of two-screen scattering within CRAFT FRBs.

In this work we measure the level of scattering and scintillation in 10 CRAFT FRBs with high spectro-temporal resolution and apply the two-screen model developed by Masui et al. (2015) and Ocker et al. (2022b) to place constraints on the distances to their respective scattering screens. In §2 we detail the data and our methodology. In §3 we present the results, and in §4 we discuss their implications.

2 METHOD

The scattering and scintillation resulting from multi-path propagation through the same medium will be related via a Fourier uncertainty relationship,

$$2\pi\nu_{\text{DC}}t_{\text{scatt}} = C. \quad (1)$$

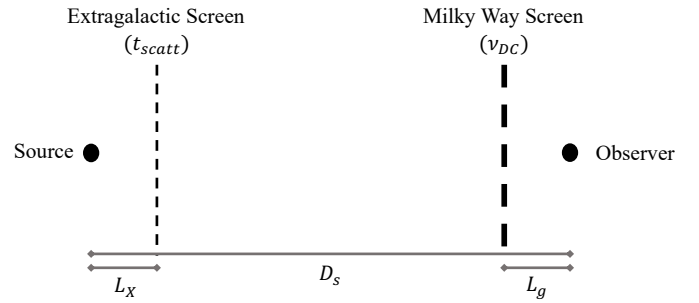


Figure 1. Diagram of the two screen scattering geometry.

The precise value of C depends on the geometry and the density fluctuations in the scattering media, however, it typically ranges between 0.5 and 2 (Lambert & Rickett 1999). As observed previously by Masui et al. (2015) and Ocker et al. (2022b), this is not always the case for FRBs, with discrepancies indicating that a single scattering medium is a poor model for propagation along the line of sight.

In these cases, a two-screen model can provide a natural explanation for the differences. Under this model, a relatively large t_{scatt} and ν_{DC} are contributed by separate screens, allowing them to be observed simultaneously for a given line of sight without violating the uncertainty relationship within a single screen. The geometry is often described as shown in Fig. 1, using L_x , the distance between the source and the first screen, and L_g , the distance between the observer and the second screen, labeled according to the expectation that the first screen is extragalactic and the second Galactic. In order for both screens to cause diffractive scintillation, the scattered image formed by the first screen must be unresolved by the second. Assuming that the distance between the scattering screens is much larger than either L_x or L_g (i.e. $(L_x + L_g)/D_s \ll 1$), this leads to the following constraint on the geometry (Ocker et al. 2022b)

$$L_x L_g \lesssim \frac{D_s^2}{2\pi\nu^2(1+z)} \frac{\nu_{\text{DC}}}{t_{\text{scatt}}}. \quad (2)$$

The factor of $(1+z)$, where z is the redshift of the source, results from using the cosmological relation between t_{scatt} and θ_{scatt} as derived in Macquart & Koay (2013). This allows the position of scattering media to be constrained directly using once-off FRBs, allowing mediums such as a diffuse IGM to be ruled out as the dominant source of scattering. In the case of FRB 201905020b, a reasonable assumption of L_g places the extragalactic screen within 100 pc of the FRB progenitor, suggesting that the scattering could be occurring in the circum-burst environment (Ocker et al. 2022b).

Our data comprise 10 localised FRBs which had been processed through the CELEBI post-processing pipeline (Scott et al. 2023) at the time of writing. These bursts were detected in real-time searches of the incoherent sum of intensities of each antenna in each of the 36 beams formed digitally using ASKAP's phased-array receivers (Bannister et al. 2017, 2019). Each detection triggered the download of the 3.1 s voltage buffers channelised using an oversampled polyphase filterbank (PFB). To localise the FRB, the voltage data are correlated, calibrated and imaged as detailed by Day et al. (2021) and exemplified in Ryder et al. (2022). To study the burst morphology, as we shall here, the PFB is inverted to recover the full ~ 3 ns time resolution of the voltage data, which are then beamformed and dedispersed as outlined in Scott et al. (2023), with the dispersion measure (DM) chosen to optimise the sharpness of temporal structures within the bursts as detailed in Sutinjo et al. (2023). We identify the bursts

within the ~ 3 s of voltage data sampled at ~ 3 ns resolution and form dynamic spectra, using a Fast Fourier Transform, of the four Stokes parameters. By default the resolution is chosen to be 0.1 MHz and 10 μ s. However, when temporal or spectral structures were found to be unresolved, respective scales as small as 1 μ s or 10 kHz were explored independently¹. Here we analyse only the Stokes I data associated with each burst; a more complete polarimetric study of each burst is reserved for a future work.

From the dynamic spectra formed, we select on and off-pulse (pre-burst) regions to account for the shape of the bandpass and to mitigate any radio frequency interference (RFI). To do this, the time-averaged spectrum in the off-pulse region is subtracted from the burst and each spectral channel in the burst is divided by the standard deviation of the corresponding off-pulse channel. The resulting burst dynamic spectrum has a noise that is normally distributed with a mean of zero and a standard deviation of unity. Furthermore, the burst intensity is now represented in units of per-channel signal-to-noise ratio (S/N).

The level of spectral modulation in a burst is calculated from the lowest, non-zero frequency lag in the mean normalised spectral auto-covariance function (ACF), as per [Macquart et al. \(2019\)](#). Bursts with a high modulation index (m) or obvious scintillation in their dynamic spectra are then investigated further. Following other studies ([Nimmo et al. 2022](#); [Ocker et al. 2022b](#)), we fit a Lorentzian to the ACF of the mean-subtracted, time-integrated, normalised burst spectra and we measure the ν_{DC} to be the half-width-half-maximum (HWHM) of the best-fit case.

In cases where significant RFI is present in the unnormalised burst dynamic spectrum, we investigate the impact of RFI subtraction on the ACF of normalised bursts. To do so, a fake FRB with a uniform spectral profile is injected into the off-pulse noise and then normalised via the same method. If a significant excess is found in the ACF of this normalised fake FRB then the RFI is deemed too significant to compensate for, and the FRB in question (or at least the section of bandwidth containing the RFI) are discarded from the sample. To avoid large Poisson noise associated with measuring only a small number of scintles (the finite scintle effect) ([Cordes et al. 1990](#)), we require the retained bandwidth to be much larger than ν_{DC} .

To distinguish scintillation from frequency structures intrinsic to the burst such as self-noise², we split the normalised FRB into four even sub-bands and fit a Lorentzian to the ACF of each band's spectrum. Due to the large number of scintles in each sub-band we expect the effect of re-binning on the results will be minimal. If ν_{DC} is observed to increase with frequency, as expected for multi-path propagation through a cold plasma, we assume the spectral structures are caused by scintillation. We characterise the minimum scintillation bandwidth we are sensitive to (ν_{min}) using simulations as described in [Appendix A](#), we highlight that this quantity is distinct from the spectral resolution of the data set.

We also fitted for t_{scatt} in each burst's frequency-integrated pulse profile. By default we assume a scattered Gaussian pulse profile, however, we allow intrinsic burst profiles to comprise multiple Gaussians when necessary. All burst morphology and ACF fitting are performed using a nested sampling technique outlined in [Qiu et al. \(2020\)](#). The frequency evolution of scattering is measured using independent fits

to burst sub-bands as done for ν_{DC} , with t_{scatt} expected to decrease at higher frequencies. Assuming that t_{scatt} and ν_{DC} evolve in frequency following a power law, we fit for a spectral index describing the evolution of each parameter (α_t and α_ν respectively), in every burst where data permits. In cases where only two sub-bands are used these spectral indices have no measured uncertainty.

We compare our measurements of scintillation or lack thereof with the expected Galactic scintillation (ν_{NE2001}) using the NE2001 electron density model ([Cordes & Lazio 2003](#)). We note that there can be order of magnitude differences in scatter broadening and scintillation bandwidths for Galactic lines of sight with the same DM ([Bhat et al. 2004](#)). Moreover, we use the best fit ν_{DC} and t_{scatt} to compute C as per [Eq. 1](#). Finally, when $C \gg 1$ we derive the two-screen distance product $L_x L_g$ as expressed in [Eq. 2](#).

3 RESULTS

The properties of each burst in our sample can be found in [Table 1](#), where a ‘-’ denotes parameters that could not be measured or derived. Within our sample, we find three FRBs with convincing evidence of spectral scintillation, from which two-screen constraints can be formed. Of the remaining FRBs, four FRBs were found to contain no spectral scintillation, two contained evidence of spectral structure that could not be confirmed as scintillation and one, FRB 20191228A, contained instrumental effects for which we could not adequately compensate. In the following sub-sections, we will describe each of these cases in greater detail, with the exception of FRB 20191228A, which is not analysed further.

3.1 FRB 20190608B

The dynamic spectrum of FRB 20190608B is shown in [Fig. 2](#) at a reduced time and frequency resolution of 0.2 ms and 2 MHz to improve visual distinction. The burst has the lowest integrated S/N in our sample, however, obvious bands of intensity can still be seen in the dynamic spectrum of the burst. The unnormalised spectrum contains negligible RFI effects and therefore we use all 336 MHz of the observed bandwidth centred at 1271.5 MHz. Analysing the time-integrated spectrum at 0.1 MHz resolution, we measure a high modulation index of $m = 0.78$ and $\nu_{\text{DC}} = 1.4 \pm 0.1$ MHz for the whole band as shown in [Fig. 3](#). Integrating over frequency, we find a scattering time of $t_{\text{scatt}} = 4.0 \pm 0.4$ ms, as shown in [Fig. 4](#).

Dividing the observation into four subbands we measure the spectral indices of ν_{dc} and t_{scatt} to be $\alpha_\nu = 5.8 \pm 0.5$ and $\alpha_t = -3 \pm 1$ respectively, as shown in [Fig. 5](#). The frequency evolution of the t_{scatt} is consistent within 1σ with $t_{\text{scatt}} \propto \nu^{-4}$ as expected for very strong scattering in a Kolmogorov turbulence with an inner scale ([Cordes & Lazio 1991](#); [Cordes & Rickett 1998](#)). Conversely, the evolution of ν_{DC} is steeper than the Kolmogorov expectation at a marginal significance of 3.6σ .

Given the high modulation index and the positive slope of ν_{DC} evolution in frequency, we assume the spectral modulation in this burst is the result of diffractive scintillation of a point-like source. Similarly, the negatively sloped frequency evolution of t_{scatt} is consistent with multi-path scattering. Combining the measurements of each over the full bandwidth we find $2\pi\nu_{\text{DC}}t_{\text{scatt}} = C \approx 35000$, indicating that a single thin screen is insufficient to describe the scattering medium along the line of sight to FRB 20190608B. Using [Eq. 2](#) we find an upper limit on the two-screen distance product of $L_x L_g \lesssim 6 \pm 1$ kpc².

¹ In these cases where greater resolution was required the spectral and temporal analyses were performed on separate data sets formed from the same voltages at independent resolutions

² Following [Ocker et al. \(2022a\)](#), we refer to frequency structures on the reciprocal scale of FRB temporal sub-structures as self-noise.

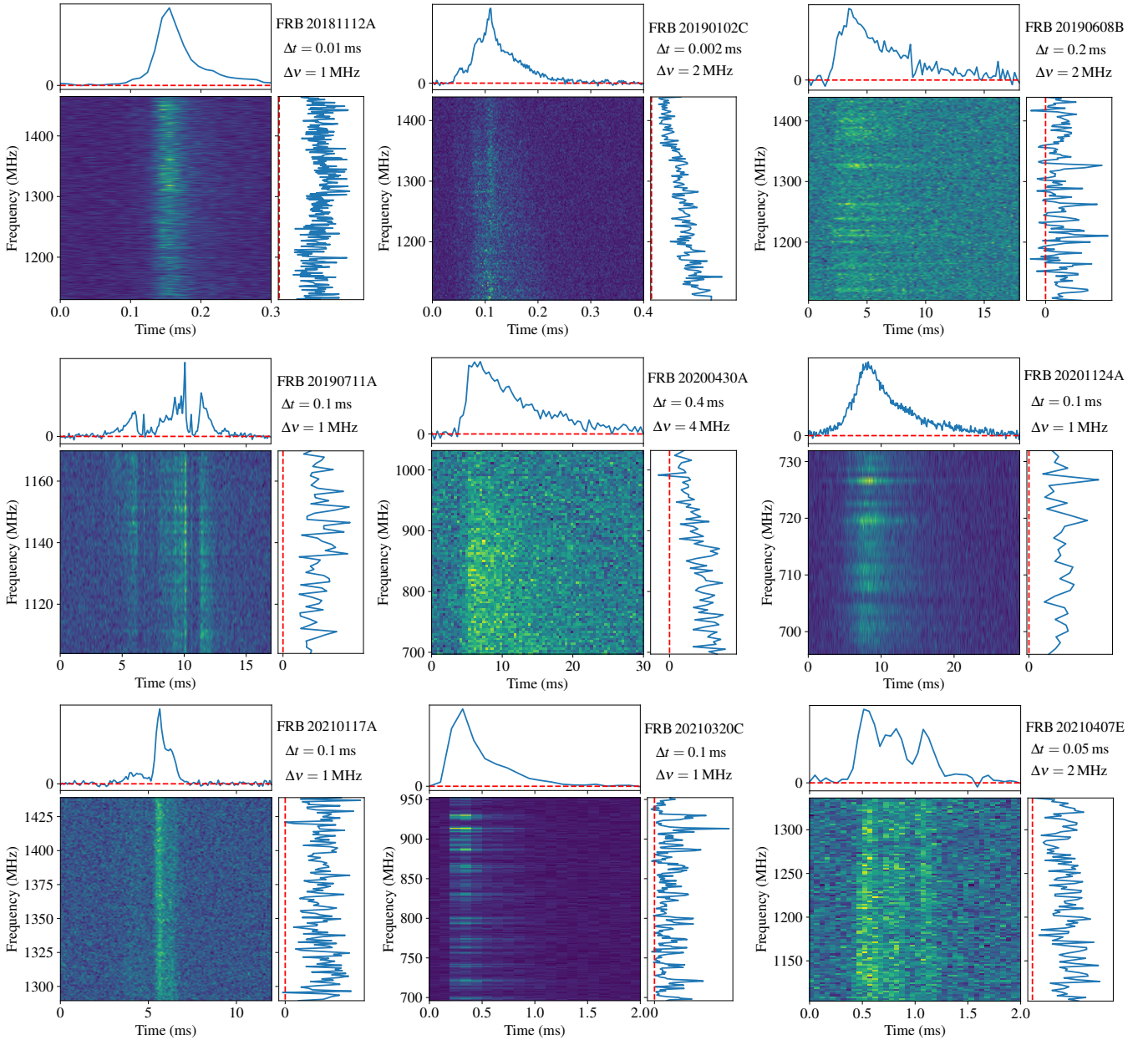


Figure 2. Dedispersed dynamic spectrum of all analysed FRBs. FRB names and spectral and temporal resolutions corresponding to the shown dynamic spectra are labelled in the top right corner of each plot. The top panels of each dynamic spectrum show the burst profiles integrated over frequency, and the right-hand panels are integrated over time.

3.2 FRB 20210320C

The dynamic spectrum of FRB 20210320C is shown in Fig. 2. The burst has $S/N = 113$ and a high modulation index of $m = 0.83$, consistent with the obvious intensity bands in the burst spectra. The de-dispersion and localisation analysis of this burst will be presented in Shannon et al. (in preparation). Due to the dispersive sweep of ~ 1.8 s across the 336 MHz ASKAP bandwidth and the ~ 1.6 s latency of the detection system, some of the FRB was lost from the voltage buffer before it was downloaded. As a result the burst emission is only found in 257 MHz of bandwidth around a central frequency 824.2 MHz. The spectral ACF is particularly well fit by a Lorentzian

profile with $\nu_{DC} = 0.91 \pm 0.03$ MHz, as seen in Fig. 3. Fig. 4 shows the best-fit model of the pulse profile, with $t_{\text{scatt}} = 0.247 \pm 0.004$ ms.

Fitting to four sub-bands, we find $\alpha_\nu = 2 \pm 1$ and $\alpha_t = -3.30 \pm 0.01$, as per Fig. 5 and 5 respectively. Each of these parameters evolves with the sign expected for multi-path propagation and are within the ranges observed for pulsars (Bhat et al. 2004). Hence we assume they are caused by scintillation and scattering respectively. Measurements over the whole band yield $C = 1410$ with an upper limit on the two-screen distance product of $L_x L_g \lesssim 550 \pm 30$ kpc².

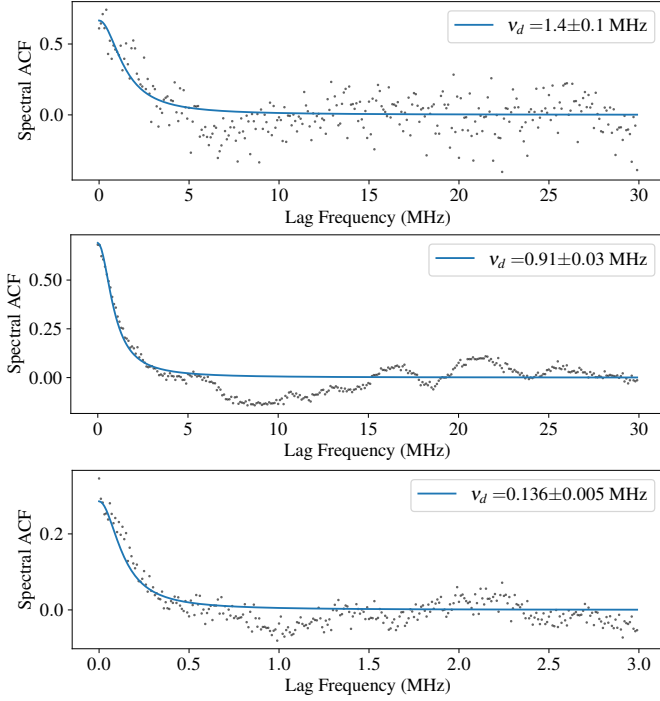


Figure 3. Scintillation fits of FRBs 20190608B, 20210320C and 20201124A from *top to bottom*. Black points show the ACF of the time-integrated burst spectra at 0.1 MHz, 0.1 MHz and 0.01 MHz resolution respectively. Blue lines show the best-fit model Lorentzians. The maximum amplitude of the ACF represents the square of the modulation index m^2 .

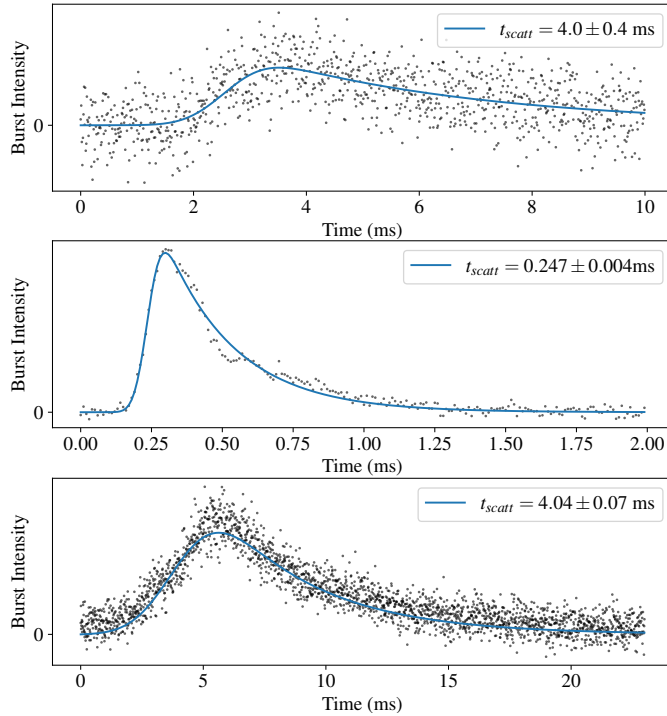


Figure 4. Scattering fits of FRBs 20190608B, 20210320C and 20201124A from *top to bottom*. Black points show the frequency-integrated pulse profiles at $10 \mu\text{s}$ resolution. The blue lines show the best-fit scattered Gaussian models.

3.3 FRB 20201124A

The dynamic spectrum of FRB 20201124A is shown in Fig. 2. The burst appears as a bright narrow-bandwidth pulse, with a $S/N = 172$.

The measured modulation index of the burst is somewhat low at only $m = 0.59$, however, the intensity banding in its spectrum motivates us to search for scintillation. To probe the fine spectral structure observed in the burst we analyse the spectrum at 0.01 MHz resolution. The Lorentzian structure expected for scintillation provides a good fit to the spectral ACF as plotted in Fig. 3, with a best fit $\nu_{\text{DC}} = 0.136 \pm 0.005$ MHz.

Despite the narrow bandwidth the burst occupies, its high S/N allows us to measure $\alpha_\nu = 10 \pm 3$ across four sub-bands as shown in Fig. 5. This spectral index is consistent with expectations at the 2σ level. The value of the decorrelation bandwidth is also consistent with the average of other measurements made for FRB 20201124A (Main et al. 2021, 2022) assuming $\alpha_\nu = 4$. We, therefore, assume that the frequency structures are caused by scintillation.

We measure the scattering time to be 4.04 ± 0.07 ms over the whole band, with a $\alpha_t = -7.3 \pm 0.9$ measured over four sub-bands as shown in Figs. 4 and 5. This measurement is steeper than the expectation at 3.7σ , however, we note that for this FRB the dynamic range in frequency is extremely limited. Assuming $\alpha_t = -4$, this measurement is consistent with previously measured upper limits on the scattering time for this source (Marthi et al. 2022).

Combined ν_{DC} and t_{scatt} over the used bandwidth yields $C \approx 3450$, indicating that a single screen is a poor model for the scattering media along the line of sight. If we assume that the initial scattering screen is unresolved by the first we constrain $L_x L_g \lesssim 1.43 \pm 0.08 \text{ kpc}^2$, however, we note that in this case, we would expect the observed FRB spectrum to be fully modulated. In §4 we consider the case of a partially resolved initial scattering screen which could explain the low modulation index.

3.4 No Observed Scintillation

For four FRBs within our sample, we observe no spectral scintillation. These are FRBs 20181112A, 20200430A, 20210117A, and 20210407E. As shown in Fig. 2, the dynamic spectra of these bursts appear spectrally smooth corresponding to relatively constant ACFs, as shown in Fig. D1 contained in the Appendix. As a result, each of these FRBs has a low modulation index, with the exception of FRB 20200430A which has a modulation index of $m = 0.45$, presumably caused by the broad spectral structure in its time-integrated spectrum which we do not attribute to scintillation. Moreover, no significant excess was seen in the spectral ACFs of these bursts at lower resolutions. We are therefore confident in the absence of spectral scintillation on frequency scales above ν_{min} for each of these FRBs, as reported in Table 1.

3.5 Anomalous

We characterise two FRBs within our sample as anomalous. These FRBs, 20190102C and 20190711A, show low spectral modulation indices associated with small excesses in their spectral ACFs. In the case of FRB 20190102C the ACF of the whole band shows a broad spectral structure which we do not associate with scintillation, and a sharper ACF peak at low spectral lags (< 5 MHz), as shown in Fig. D3, which is potentially consistent with scintillation. We fail to find an ACF excess when we decompose the burst into four sub-bands, however, reducing the division to two sub-bands yields a reasonable fit as shown in Fig. D3. Derived ν_{DC} values evolve in the expected

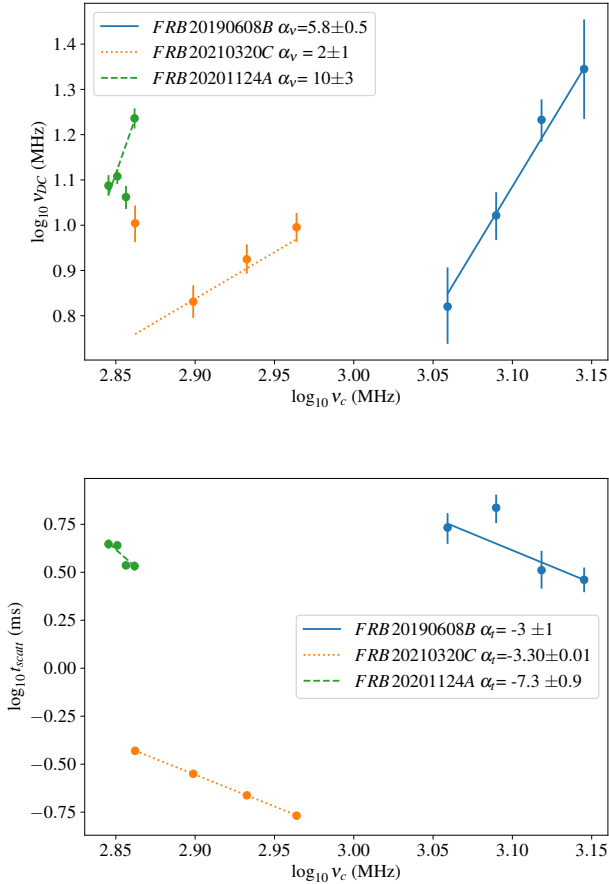


Figure 5. Frequency evolution of ν_{DC} (top) and t_{scatt} (bottom) modelled from sub-band analysis of each scintillating FRB. The lines show the best-fit power-law models for each case.

direction for scintillation, however, given the low number of sub-bands we are unable to estimate the error on the spectral index of $\alpha_\nu = 10$.

In the case of FRB 20190711A the ACF is well fit by the expected lorentzian form of scintillation, as shown in Fig. D2. Analysis of the sub-bands measures $\alpha_\nu = -10 \pm 5$, contrary to the expectation for scintillation decorrelation bandwidths to increase in size with frequency. We highlight however the low fractional bandwidth (≈ 0.06) over which these data are measured.

Both FRBs show complex pulse profiles, with multiple components. Owing to the computational load associated with multi-component fitting we only model the temporal properties of each of these bursts with two sub-bands. In each case the short timescale structure of each of these bursts could also cause intrinsic spectral structure on the reciprocal scale (Nimmo et al. 2022). Given the uncertainty associated with their measurements and the low C values, which can indicate the consistency of spectral structures with self-noise, we conclude that there is insufficient evidence to prove scintillation in these cases.

4 DISCUSSION

For the cases where we find convincing evidence for scintillation and pulse broadening, i.e. FRBs 20190608B, 20201124A, and 20210320C, the scattering geometry is constrained by the $L_x L_g$ product upper limit. FRBs 20190608B and 20201124A provide particularly tight constraints.

4.1 FRB 20190608B

Due to limitations in spectral resolution, the presence of diffractive scintillation was unable to be confirmed in a previous analysis of FRB 20190608B (Day et al. 2020). Without the presence of this scintillation the position of the screen causing temporal scattering in the burst had to be inferred indirectly from estimates of the host galaxy properties (Chittidi et al. 2021) and the properties of the cosmic web along the FRB line of sight (Simha et al. 2020). The joint conclusion of these studies is that the temporal scattering in FRB 20190608B is likely contributed by a region within the host galaxy as there are no cosmic web structures or foreground galaxies intersecting the line of sight sufficiently to explain the large scattering time.

By confirming scintillation and placing an upper limit of $L_x L_g \lesssim 6 \pm 1 \text{ kpc}^2$ our results provide a direct constraint on the scattering geometry. For similar values $L_x \approx L_g$, the screens must be contained within the host and Milky Way galaxies respectively.

By measuring the angular broadening extent of an FRB using VLBI (very long baseline interferometry), the effective distance to the relevant scattering screen can be determined (Ocker et al. 2021). This has been done for FRB 20121102 using the European VLBI network (Marcote et al. 2017). The effective distance to its Galactic scattering screen is constrained to be consistent with a peak in differential scattering measure associated with a sharp change in electron density predicted by the NE2001 model Ocker et al. (2021). Fig. 6 shows the C_n^2 and differential DM estimated for each of our scintillating FRB lines of sight. Using the peak in C_n^2 , corresponding to a sharp change in differential DM, we estimate $L_g \approx 0.36 \text{ kpc}$, corresponding to $L_x \lesssim 16.7 \text{ kpc}$. This region corresponds to the host galaxy of FRB 20190608B and therefore our direct constraints support the conclusions of Simha et al. (2020); Chittidi et al. (2021). Additionally, by assuming $L_g \approx 0.36 \text{ kpc}$, ν_{DC} and the fully modulate version of Eq. B4 can be used to constrain the product

$$t_{\text{scatt}}(1+z_d) \frac{D_{ds,x}}{D_{d,x}} \lesssim \frac{\nu_{\text{DC}} D_s}{2\pi v^2 L_g} \quad (3)$$

where $D_{d,x}$ is the distance to the extragalactic scattering screen at redshift z_d , and $D_{ds,x}$ is the distance between the screen and the host. From this constraint, we place an upper limit on the amount of scattering caused by the IGM. In the case of FRB 20190608B, we find $t_{\text{scatt}}(1+z_d)D_{ds,x}/D_{d,x} \lesssim 1.7 \times 10^{-7} \text{ s}$, corresponding to less than $0.43 \mu\text{s}$ of scattering at 1 GHz (assuming a ν^{-4} scaling), for a screen at redshift $z \approx 0.056$, where $D_{ds,x}/D_{d,s} \approx 1$ and the scattering time associated with a given scattering measure is maximised (Macquart & Koay 2013).

4.2 FRB 20210320C

FRB 20210320C provides perhaps our sample’s best example of scattering and scintillation, with the burst morphologies presented in Fig. 3 and Fig. 4 showing good agreement with the expected shapes and frequency evolutions for diffractive scintillation and pulse broadening. The small amount of observed scattering in this case, how-

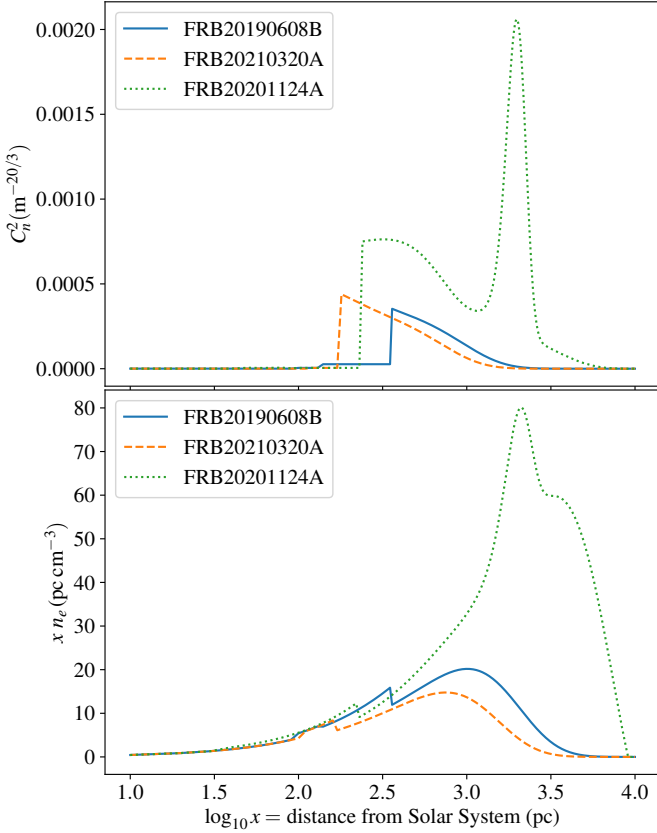


Figure 6. *Top:* The expected differential scattering measure contributed by the Milky Way for scintillating FRB lines of sight as calculated from the NE2001 model (Cordes & Lazio 2003). *Bottom:* For the same lines of sight, the expected contribution to DM as a function of $\log_{10} x$ where x is the distance from the Solar system. For each FRB line of sight the maximum of C_n^2 occurs at 0.36 kpc, 0.18 kpc, and 1.98 kpc respectively, corresponding to sharp changes in DM contribution.

ever, results in only a loose constraint on the scattering geometry of $L_x L_g \lesssim 550 \pm 30 \text{ kpc}^2$. From Fig. 6 the peak in turbulence strength is close to the observer at a distance of 0.18 kpc, which corresponds to $L_x \lesssim 3000 \text{ kpc}$. As such, the scattering cannot be definitively constrained to the host galaxy. We note however, that the observed scattering must still be occurring within the first $\approx 0.3\%$ of the total path length from the host and so cannot be due to some diffuse component of the IGM as its contribution to the scattering would characteristically peak halfway between the source and the observer. For IGM scattering in general, by assuming $L_g \approx 0.18 \text{ kpc}$, we find $t_{\text{scatt}} D_{ds,x}/D_{d,x} \lesssim 1.1 \times 10^{-6} \text{ s}$, using Eq. 3. This corresponds to less than $0.44 \mu\text{s}$ of scattering at 1 GHz (assuming a ν^{-4} scaling), for a screen at redshift $z \approx 0.126$, where $D_{ds,x}/D_{d,s} \approx 1$.

The host galaxy localisation image of FRB 20210320C, shows a faint object nearby to the line of sight. The redshift of this object has yet to be determined, however, if it lies foreground to the host galaxy at a similar redshift it may be the source of the observed scatter broadening.

4.3 FRB 20201124A

Conversely to the other scintillating FRBs in our sample, FRB 20201124A is a closely studied repeating FRB with existing

measurements for its scattering time and decorrelation bandwidth. Analysis by Main et al. (2021) measured $\nu_{\text{DC}} \approx 0.1 \text{ MHz}$ and $t_{\text{scatt}} \approx 11 \text{ ms}$ at a central frequency of 575 MHz. Substituting these values into Eq. 2 yields $L_x L_g \lesssim 0.6 \text{ kpc}^2$, which is tighter than the limit we derive, $L_x L_g \lesssim 1.43 \pm 0.08 \text{ kpc}^2$, consistent with the expected steep frequency dependence of the constraints (Main et al. 2021).

Despite the evidence for scintillation, the observed modulation index of FRB 20201124A remains too low to be consistent with the full modulation expected for diffractive scintillation of a point-like source. In this context, a source will be considered point-like if it satisfies Eq. C1. If the equation is violated, we enter the regime of diffractive scintillation of an extended source. Here, the modulation index of the spectral scintillation will begin to decrease as the angular extent of the scattering disk of the first screen increases (Narayan 1992). Within the temporal profile of scattered bursts, later times are associated with larger angular extents in the scattering disk. Similarly to the analysis of Masui et al. (2015), we can analyse the modulation index of the burst as a function of time to identify whether the entire angular extent of the scattered image undergoes the same scintillation. If the scattered image associated with the observed temporal broadening is responsible for the suppression of Galactic scintillation, we expect that the later parts of the burst, with larger angular extents, will show lower modulation indices. Fig. 7 shows the evolution of the modulation index over the duration of the burst in increments of 0.1 ms. At each increment a 1 ms wide boxcar of the burst’s dynamic spectrum is used to calculate the modulation index, effectively smoothing the result to boost S/N . As seen in Fig. 7 the modulation index shows a small decrease of ~ 0.2 over the main component of the burst profile with a large variance in m_g displayed on either side of the burst as S/N decreases. A linear model shows reasonable agreement with the data, as would be expected for a circularly symmetric scattered image, where separation in time is linearly proportional to angular offset. The low modulation index of spectral scintillation in FRB 20201124A may, therefore, indicate that the scattering screen at the host is partially resolved by the Milky Way scattering screen.

For the fully modulated case, the coherence length of a wave incident on the second screen can only be constrained to be larger than the projected scattering angle length. In the partially resolved case, however, it can be solved for exactly using the modulation index. This, in turn, allows the two-screen distance product to be specified exactly, as, (see B for derivation)

$$L_x L_g \approx \frac{D_s^2}{2\pi\nu^2(1+z)} \frac{\nu_{\text{DC}}}{m_g^2 t_{\text{scatt}}}, \quad (4)$$

where m_g is the modulation index of the Galactic screen. Solving this for the case of FRB 20201124A indicates that the two-screen distance product should be equal to $L_x L_g \approx 4 \text{ kpc}^2$.

A recent study of the annual variation of scintillation in FRB 20201124A has revealed that the scattering screen contributing the observed Galactic scintillation is much closer than the peak in C_n^2 at $\sim 2 \text{ kpc}$ suggests, located at around $L_g = 0.40 - 0.46 \text{ kpc}$, depending on the isotropy of the screen (Main et al. 2022). We discuss the potential impact of screen anisotropy in appendix C. Taking the case of the uniform two-dimensional screen, $L_g = 0.46 \text{ kpc}$, we can approximate the distance between the source and host screen to be $L_x \approx 9 \text{ kpc}$, which is greater than the optical extent of the host galaxy (Xu et al. 2022). This indicates that, if the angular broadening associated with the measured scattering tail is suppressing the observed Galactic scintillation, that scattering is likely occurring in

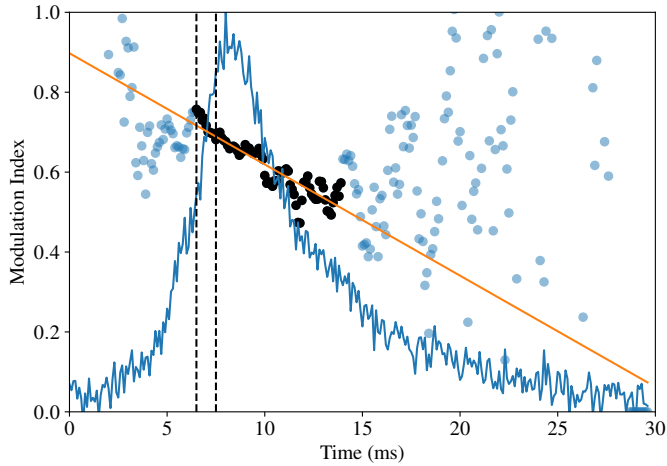


Figure 7. Modulation index of FRB 20201124A as a function of time. Scatter points show the modulation index calculated for the burst spectrum at a resolution of 0.01 MHz integrated over 1 ms of the bursts time profile (shown by the blue line) beginning at the time marked by the point. The dotted black lines depict the area of integration in time. The linear model of modulation index decay is shown by the orange line. The points used in the fit are shown in black.

the halo of the galaxy, rather than in the circum-burst environment or the host ISM.

The low modulation index of the burst could also be caused by angular broadening from a third screen along the line of sight which contributes negligibly to the observed scattering and scintillation of the burst. This is precisely the inverse of the case discussed in §4.1 regarding limits on IGM scattering. The two possible locations for this potential third screen are within the Milky Way or the IGM. The case where the third screen is also within the host galaxy is captured implicitly by the above discussion. Already, some motivation for a third screen within the Milky Way exists, in the form of the peak in C_n^2 at ≈ 2 kpc shown in Fig. 6, which we know is not associated with the observed scintillation. The scattering time required from the third screen to reduce the modulation index of the Galactic scintillation is given by

$$t_{\text{scatt}} \approx \frac{\nu_{\text{DC}} D_{d,x}}{2\pi\nu^2 m_g^2 L_g}, \quad (5)$$

adapted from Eq. 3. Solving for $m_g = 0.59$ yields $t_{\text{scatt}} \approx 1.3 \times 10^{-7} \mu\text{s}$ at 1 GHz (assuming a ν^{-4} scaling), showing that the foreground Galactic scintillation can be suppressed with very little additional scattering from a third screen in the Milky Way. From this result, we conclude that while it is possible for such a scenario to be true, it is more likely that any third screen in the Milky Way would completely suppress the scintillation from the foreground screen at 0.46 kpc and is therefore inconsistent with our observations.

If the third screen is instead placed within the IGM, we can use the inverse of Eq. 3, dividing the right-hand side by m_g^2 to take the partial modulation into account. This yields $t_{\text{scatt}}(1+z_d)D_{ds,x}/D_{d,x} \approx 0.027 \mu\text{s}$ at 1 GHz (assuming a ν^{-4} scaling), we plot this result as a function of $D_{d,x}$ in Fig. D4. The scattering times required to cause $m_g = 0.59$ are reasonable expectations for scattering from the IGM (Macquart & Koay 2013) and would be invisible in the temporal profile of the burst. The range of decorrelation bandwidths corresponding to the spectral scintillation also imposed by an IGM screen, however, falls mostly within our detectable range and therefore should

appear in our observations. As a result we find it unlikely that angular broadening from a third screen in the IGM can adequately explain the observed scintillation modulation. We note however that for IGM screens closer than 50 Mpc the decorrelation bandwidth would be greater than our observed bandwidth, and therefore undetectable.

Given the issues outlined above with a third screen interpretation, coupled with the observed evolution of the modulation index over the burst, we tentatively conclude that the most likely scenario is that the Galactic scintillation observed in the burst is suppressed by the angular broadening corresponding to the observed temporal broadening. As such FRB 20201124A is a potential candidate of interest for probing the CGM, and we recommend its modulation index and scattering times be studied in detail in future statistical studies of its repeating bursts.

4.4 Circum-burst Scattering

Given the localisation of the scattering to within 0.4 AU of the source for FRB 20190520B (Ocker et al. 2022a), it is prudent to consider the ramifications if this were typical for all FRBs. The extremely low value of L_x in each case would leave $L_g \lesssim D_s$, and hence the position of the screen responsible for the spectral scintillation would be unbounded. While the diffuse IGM is not expected to cause sufficient scattering to account for FRB temporal broadening, it is expected to be able to cause the microsecond level scattering required to see scintillation on megahertz scales (Macquart & Koay 2013). It is, therefore, possible, if the screen causing the observed temporal broadening of FRBs is associated with the circum-burst environment, that the observed spectral scintillation could come from the IGM, invalidating the previous IGM scattering constraints in §4.1 and 4.2. However, in order for no additional scintillation from the Milky Way to be observed, consistent with our observations, which show only one scale of frequency modulation, the angular broadening from the IGM must be such that any subsequent Milky Way scintillation is suppressed.

The two-screen interaction between the IGM and the Milky Way, can be considered using Eq. 3 where $t_{\text{scatt}} = 1/2\pi\nu_{\text{DC}}$ and $D_{ds,x} = D_{d,x}$, and assuming that the Milky Way scintillates as expected by NE2001, Galactic scintillation will be suppressed for all

$$L_g \gtrsim \frac{D_s}{\nu^2(1+z_d)} \nu_{\text{DC}} \nu_{\text{NE2001}}, \quad (6)$$

where z_d is the redshift of the IGM screen. For FRBs 20190608B and 20210320C, Eq. 6 yields $L_g \gtrsim 1$ kpc. Fig. 6 shows that for both FRBs, the Galactic scattering screens are expected to be closer than 1 kpc, and therefore would still cause visible scintillation in each, in addition to the IGM scintillation. This is inconsistent with our observations, and therefore we find it unlikely that the observed scintillation comes from the IGM. This agrees with the observed correlation between FRB scintillation and expectations from Galactic electron distribution models (Schoen et al. 2021). We highlight, however, that scintillation from the IGM is a reasonable possibility for FRBs that appear sufficiently point-like. To investigate this possibility further we recommend a statistical study that measures the correlation between FRB redshift and ν_{DC} . The use of redshift is preferable to dispersion measure as the host contribution to dispersion is difficult to separate from the IGM contribution. If a significant fraction of FRBs contain scintillation from the IGM, we expect that an anti-correlation between redshift and ν_{DC} will be present.

to limits proportional to SM_{eff} . For the case of a diffuse IGM, [Macquart & Koay \(2013\)](#) show that SM_{eff} should be a monotonically increasing function of redshift, which is inconsistent with the limits we derive, as shown in Fig. D5. As a result, a diffuse IGM component cannot be responsible for suppressing Galactic scintillation expected from NE2001 in our non-scintillating bursts given our observations of scintillation in others. We, therefore, suggest that it is unlikely that angular broadening associated with scattering from the diffuse IGM, or regions within the host galaxy of each burst is suppressing the Galactic scintillation of the non-scintillating FRBs in our sample. Rather, it is more likely that either 1) the true scintillation bandwidths are different from that predicted under the NE2001 and YMW16 models, similar to the case of FRB 20201124A, or 2) significant structures in the IGM, such as a galaxy halo, are intervening between the source and the observer, resulting in significant angular broadening. In the case of FRB 20181112A such a structure exists in the form of a foreground galaxy intervening at $z = 0.36738$ ([Prochaska et al. 2019](#)). However, at this redshift a screen contributing the maximum amount of scattering allowed for this burst (0.0278 ms, as per Table 1) results in a modulation index of $m_g = 0.46$ and should be visible in its ACF (see Fig. D1).

As demonstrated in [Morgan et al. \(2022\)](#), there exists a strong correlation between the angular broadening of extragalactic point sources and the intensity of Galactic $H\alpha$ emissions. Angular broadening of extragalactic sources is weighted approximately uniformly with distance for Galactic scattering screens ([Cordes & Lazio 2003](#)), and therefore, ionised regions, shown by Galactic $H\alpha$ observations, are expected to contribute significantly to angular broadening by the ISM. Conversely, the scintillation bandwidths and scattering times associated with the ISM are weighted more heavily towards the middle of the path length ([Cordes & Lazio 2003](#)), allowing background regions of lower $H\alpha$ intensity to cause greater scattering times than more intense foreground regions, confusing any correlation. Moreover, close to the Galactic plane the ionised region responsible for the observed scattering may not be visible in $H\alpha$, due to extinction ([Finkbeiner 2003](#)). As such, we do not necessarily expect to observe a strong correlation between FRB ν_{DC} and $H\alpha$. The association of scintillation in FRB 20201124A to a more local screen, however, does provide some motivation to search for scintillation screens locally, where extinction should be relatively low. Thus, we also compare scintillation in our sample to a Galactic map of $H\alpha$ intensity ([Finkbeiner 2003](#)) as shown in Fig. 8. We find no obvious relation between scintillating and non-scintillating FRBs and $H\alpha$ intensity or variance in $2.5^\circ \times 2.5^\circ$ area surrounding each FRB line of sight. We note, however, that the size of a reasonable scattering disk lies well below the resolution of data used to compose this map and therefore may show correlation with smaller scale $H\alpha$ structures.

5 CONCLUSION

The location of the dominant scattering screens contributing to the temporal broadening and spectral scintillation of FRBs has important ramifications for many areas of astrophysics. Scattering near the host galaxy or circum-burst environments, such as FRB 20190520B affects our understanding of progenitor evolution; scattering in intervening galaxies could constrain the presence of cold cloudlets in the CGM; finally, scattering in our own Galaxy could inform models of the Galactic electron distribution. For apparently non-repeating FRBs scattering can be difficult to localise, but if bursts are observed to scatter and scintillate independently then a two-screen model can be used to make direct constraints.

In this work, we have measured the level of scattering and scintillation in 10 CRAFT FRBs with high spectro-temporal resolution and applied the two-screen model developed by [Masui et al. \(2015\)](#) and [Ocker et al. \(2022b\)](#) to place constraints on the distances to their respective scattering screens. We find strong evidence for scattering and scintillation in three FRBs, and strong evidence for no spectral modulation in four FRBs. The remaining are indeterminate. Of the scintillating FRBs the scattering in FRB 20190608B is robustly associated with the host galaxy in agreement with previous estimates; the scattering in FRB 20210320C must occur within 3 Mpc of the host; finally, we find that the scattering in FRB 20201124A is likely associated with its host galaxy environment, however, the low modulation index of its Galactic scintillation suggests the dominant scattering region may be in the halo rather than the host ISM. The Galactic scintillation of FRBs 20190608B and 20210320C are in general agreement with the scintillation expected from Galactic models YMW16 ([Yang & Zhang 2017](#)) and NE2001 ([Cordes & Lazio 2003](#)). However, the anomalously low scattering of FRB 20201124A and the definitive lack of scintillation in four FRBs indicates that, if the observed pulse broadening is contributed by host galaxy ISMs or circum-burst environments, existing models may be poor estimators of the scattering times associated with the Milky Way's ISM, as has been noted already by [Ocker et al. \(2021\)](#) in the case of YMW16. Additionally, we find no obvious relationship with the large-scale mean and variance of surrounding Galactic $H\alpha$ emission. We leave a statistical comparison of scintillation quantities with other burst and host galaxy properties to a future study, once the sample of high-resolution bursts has been expanded.

With the automated CELEBI post-processing pipeline now operational and the CRAFT Coherent upgrade expected soon we expect that the number of observed scintillating FRBs will grow, allowing for a statistical study of their Galactic and extragalactic screen properties. Furthermore, we highlight that targeting low Galactic latitudes for FRB searches may further increase the number of observed, strongly scintillating FRBs, allowing for the stronger constraint of their extragalactic counterparts and Galactic electron distribution models.

ACKNOWLEDGEMENTS

We would like to acknowledge A/Prof. Kiyoshi Masui for refereeing this manuscript and providing helpful insights related to the evolution of spectral modulation indices in bursts undergoing multipath scattering. CMT is supported by an Australian Research Council Future Fellowship under project grant FT180100321. ATD acknowledges support from the Australian Government through the Australian Research Council's Discovery Projects funding scheme (project ID DP220102305). KG acknowledges support through Australian Research Council Discovery Project DP200102243. CWJ and MG acknowledge support by the Australian Government through the Australian Research Council's Discovery Projects funding scheme (DP210102103). RMS acknowledges support through Australian Research Council Future Fellowship FT190100155 and Discovery Project DP220102305.

DATA AVAILABILITY

The data underlying this article will be shared upon reasonable request to the corresponding author.

REFERENCES

- Anna-Thomas R., et al., 2022, A Highly Variable Magnetized Environment in a Fast Radio Burst Source, <http://arxiv.org/abs/2202.11112>
- Bannister K., et al., 2017, *The Astrophysical Journal*, 841, L12
- Bannister K. W., et al., 2019, *Science*, 365, 565
- Bartel N., Burgin M. S., Fadeev E. N., Popov M. V., Ronaghikhameneh N., Smirnova T. V., Soglasnov V. A., 2022, *The Astrophysical Journal*, 941, 112
- Bhat N. D. R., Rao A. P., Gupta Y., 1999, *The Astrophysical Journal Supplement Series*, 121, 483
- Bhat N. D. R., Cordes J. M., Camilo F., Nice D. J., Lorimer D. R., 2004, *The Astrophysical Journal*, 605, 759
- Brisken W. F., Macquart J.-P., Gao J. J., Rickett B. J., Coles W. A., Deller A. T., Tingay S. J., West C. J., 2010, *The Astrophysical Journal*, 708, 232
- Chawla P., et al., 2022, *The Astrophysical Journal*, 927, 35
- Chittidi J. S., et al., 2021, *The Astrophysical Journal*, 922, 173
- Cho H., et al., 2020, *The Astrophysical Journal*, 891, L38
- Connor L., et al., 2020, *Monthly Notices of the Royal Astronomical Society*, 499, 4716
- Connor L., et al., 2023, Deep Synoptic Array science: Two fast radio burst sources in massive galaxy clusters, [doi:10.48550/arXiv.2302.14788](https://doi.org/10.48550/arXiv.2302.14788), <http://arxiv.org/abs/2302.14788>
- Cordes J., Lazio T., 1991, *ApJ*, 376, 123
- Cordes J. M., Lazio T. J. W., 2001, *The Astrophysical Journal*, 549, 997
- Cordes J. M., Lazio T. J. W., 2003, NE2001.I. A New Model for the Galactic Distribution of Free Electrons and its Fluctuations, [doi:10.48550/arXiv.astro-ph/0207156](https://doi.org/10.48550/arXiv.astro-ph/0207156), <http://arxiv.org/abs/astro-ph/0207156>
- Cordes J. M., Rickett B. J., 1998, *The Astrophysical Journal*, 507, 846
- Cordes J. M., Wolszczan A., Dewey R. J., Blaskiewicz M., Stinebring D. R., 1990, *The Astrophysical Journal*, 349, 245
- Cordes J. M., Ocker S. K., Chatterjee S., 2022, *The Astrophysical Journal*, 931, 88
- Day C. K., et al., 2020, [arXiv:2005.13162](https://arxiv.org/abs/2005.13162) [astro-ph]
- Day C. K., Deller A. T., James C. W., Lenc E., Bhandari S., Shannon R. M., Bannister K. W., 2021, *Publications of the Astronomical Society of Australia*, 38, e050
- Farah W., et al., 2018, *Monthly Notices of the Royal Astronomical Society*, 478, 1209
- Finkbeiner D. P., 2003, *The Astrophysical Journal Supplement Series*, 146, 407
- Gupta V., Flynn C., Farah W., Bailes M., Deller A. T., Day C. K., Lower M. E., 2022, *Monthly Notices of the Royal Astronomical Society*, 514, 5866
- Hilmarsson G. H., et al., 2021, *The Astrophysical Journal Letters*, 908, L10
- Lambert H. C., Rickett B. J., 1999, *The Astrophysical Journal*, 517, 299
- Lorimer D. R., Bailes M., McLaughlin M. A., Narkevic D. J., Crawford F., 2007, *Science (New York, N.Y.)*, 318, 777
- Macquart J.-P., Koay J. Y., 2013, *The Astrophysical Journal*, 776, 125
- Macquart J.-P., Shannon R. M., Bannister K. W., James C. W., Ekers R. D., Bunton J. D., 2019, *The Astrophysical Journal*, 872, L19
- Macquart J.-P., et al., 2020, *Nature*, 581, 391
- Main R. A., Hilmarsson G. H., Marthi V. R., Spitler L. G., Wharton R. S., Bethapudi S., Li D. Z., Lin H.-H., 2021, *Monthly Notices of the Royal Astronomical Society*, 509, 3172
- Main R. A., Bethapudi S., Marthi V. R., Bause M. L., Li D. Z., Lin H.-H., Spitler L. G., Wharton R. S., 2022, Modelling Annual Scintillation Velocity Variations of FRB 20201124A, [doi:10.48550/arXiv.2212.04839](https://doi.org/10.48550/arXiv.2212.04839), <http://arxiv.org/abs/2212.04839>
- Marcote B., et al., 2017, *The Astrophysical Journal Letters*, 834, L8
- Margalit B., Metzger B. D., 2018, *The Astrophysical Journal*, 868, L4
- Marthi V. R., et al., 2022, *Monthly Notices of the Royal Astronomical Society*, 509, 2209
- Masui K., et al., 2015, *Nature*, 528, 523
- McCourt M., Oh S. P., O'Leary R., Madigan A.-M., 2018, *Monthly Notices of the Royal Astronomical Society*, 473, 5407
- Michilli D., et al., 2018, *Nature*, 553, 182
- Morgan J. S., Chhetri R., Ekers R., 2022, *Publications of the Astronomical Society of Australia*, 39, e063
- Narayan R., 1992, *Philosophical Transactions of the Royal Society of London Series A*, 341, 151
- Nicastro L., Nigro F., D'Amico N., Lumiella V., Johnston S., 2001, *Astronomy & Astrophysics*, 368, 1055
- Nimmo K., et al., 2022, *Nature Astronomy*, 6, 393
- Ocker S. K., Cordes J. M., Chatterjee S., 2021, *The Astrophysical Journal*, 911, 102
- Ocker S. K., Cordes J. M., Chatterjee S., Li D., Niu C. H., McKee J. W., Law C. J., Anna-Thomas R., 2022a, Scattering variability detected from the circumsource medium of FRB 20190520B, [doi:10.48550/arXiv.2210.01975](https://doi.org/10.48550/arXiv.2210.01975), <http://arxiv.org/abs/2210.01975>
- Ocker S. K., et al., 2022b, *The Astrophysical Journal*, 931, 87
- Prochaska J. X., Neeleman M., 2018, *Monthly Notices of the Royal Astronomical Society*, 474, 318
- Prochaska J. X., et al., 2019, [arXiv:1909.11681](https://arxiv.org/abs/1909.11681) [astro-ph]
- Qiu H., et al., 2020, *Monthly Notices of the Royal Astronomical Society*, 497, 1382
- Rickett B., 2006, *Chinese Journal of Astronomy and Astrophysics*, 6, 197
- Ryder S. D., et al., 2022, Probing the distant universe with a very luminous fast radio burst at redshift 1, [doi:10.48550/arXiv.2210.04680](https://doi.org/10.48550/arXiv.2210.04680), <http://arxiv.org/abs/2210.04680>
- Schoen E., et al., 2021, *Research Notes of the AAS*, 5, 271
- Scott D. R., et al., 2023, [10.48550/arXiv.2301.13484](https://doi.org/10.48550/arXiv.2301.13484)
- Simha S., et al., 2020, *The Astrophysical Journal*, 901, 134
- Stinebring D. R., 2006, *Chinese Journal of Astronomy and Astrophysics*, 6, 204
- Sutinjo A. T., et al., 2023, Calculation and Uncertainty of Fast Radio Burst Structure Based on Smoothed Data, <http://arxiv.org/abs/2302.06220>
- Thornton D., et al., 2013, *Science*, 341, 53
- Trang F. S., Rickett B. J., 2007, *The Astrophysical Journal*, 661, 1064
- Vedantham H. K., Phinney E. S., 2019, *Monthly Notices of the Royal Astronomical Society*, 483, 971
- Wang Y., Tuntsov A., Murphy T., Lenc E., Walker M., Bannister K., Kaplan D. L., Mahony E. K., 2021, *Monthly Notices of the Royal Astronomical Society*, 502, 3294
- Xu H., et al., 2022, *Nature*, 609, 685
- Yang Y.-P., Zhang B., 2017, *The Astrophysical Journal*, 847, 22

FRB	S/N	m	ν_c (MHz)	ν_{DC} (MHz)	t_{scatt} (ms)	C	α_ν	α_t	ν_{Ne2001} (MHz)	ν_{min} (MHz)	$L_x L_g$ (kpc ²)
20181112A	143	0.1	1297.5	-	.0278 ± 0.0008	-	-	-0.8 ± 0.6	2.82	0.001	-
20190102C	124	0.41	1271.5	0.6 ± 0.3	0.046 ± 0.001	170	10	-4	1.26	0.001	-
20190608B	32.9	0.78	1271.5	1.4 ± 0.1	4.0 ± 0.4	35000	5.8 ± 0.5	-3 ± 1	3.08	1	6 ± 1
20190711A	89.3	0.64	1136.9	0.11 ± 0.01	0.008 ± 0.003	6	-10 ± 5	-10	0.837	0.0001	-
20191228A	51.1	0.77	1340.3	-	5.5 ± 0.2	-	-	-	5.47	0.1	-
20200430A	56.7	0.45	864.5	-	7.7 ± 0.5	-	-	-3.0 ± 0.3	0.973	0.1	-
20201124A	172	0.59	713.9	.136 ± 0.005	4.04 ± 0.07	3450	10 ± 3	-7.3 ± 0.9	0.00721	1 × 10 ⁻⁴	1.43 ± 0.08
20210117A	43.9	0.0	1364.2	-	0.14 ± 0.6	-	-	1 ± 4	5.82	0.1	-
20210320C	113	0.83	824.2	0.91 ± 0.03	0.247 ± 0.004	1410	2 ± 1	-3.30 ± 0.01	1.03	0.1	550 ± 30
20210407E	49.7	0.0	1220.2	-	0.090 ± 0.010	-	-	-	3.01	1	-

Table 1. Measured scintillation parameters for a sample of localised CRAFT FRBs

APPENDIX A: SIMULATING SPECTRAL SCINTILLATION DETECTION THRESHOLD

We create a blank spectrum with 336 MHz of bandwidth around a central frequency of 1271.5 MHz at 0.1 MHz resolution. We then populate it with $N = f \times 336 / \nu_{\text{DC},0}$ scintles, where the filling fraction f is 0.5, a typical assumption for pulsar scintillation (Bhat et al. 1999; Nicastro et al. 2001) and $\nu_{\text{DC},0}$ is the decorrelation bandwidth of the simulated burst at 1 GHz. The amplitude of the scintles is set such that the sum of the noiseless spectrum is equal to the simulated burst's S/N and their positions in frequency (ν_p) are drawn randomly from a uniform distribution. The scintles are Lorentzian in shape with a HWHM of $2\nu_{\text{DC}}$ (Bartel et al. 2022), corresponding to a decorrelation bandwidth of $\nu_{\text{DC}} = \nu_{\text{DC},0}(\nu_p/1 \text{ GHz})^4$. These arrays represent the noise-free signal (S) of a burst. We also construct noise arrays (N) filled with white noise following a $N(0, 1/\sqrt{3360})$ distribution.

We simulate 1000 signal and noise arrays for each of a range of combinations of S/N and ν_{DC} values. For each, we calculate the ACF signal and noise as

$$\text{ACF}_S(j) = \sum_{i=0}^{3360} S(i)S(i+j) \quad (\text{A1})$$

$$\text{ACF}_N(j) = \sum_{i=0}^{3360} S(i)N(i+j) + S(i+j)N(i) + N(i)N(i+j). \quad (\text{A2})$$

The χ^2 value for the significance of the burst ACF at a given S/N and ν_{DC} is then calculated as

$$\chi^2 = \sum_{j=0}^{3360} \frac{\overline{\text{ACF}_S(j)} - \overline{\text{ACF}_N(j)}}{\sigma(j)}, \quad (\text{A3})$$

where the bar represents the mean over the 1000 simulated instances and $\sigma(j)$ is the standard deviation of $\text{ACF}_N(j)$. Due to the high degree of freedom of the χ^2 distribution (roughly equal to the number of channels, 3360) the probability of chance significance ($p = 1 - \text{CDF}(\chi^2)$) also transitions sharply from ≈ 1 to ≈ 0 and hence we set the detection threshold at this transition at χ^2 value of ≈ 3360 . Fig. A1 depicts the simulated χ^2 values and over-plots the detection threshold from linear fit in log space to the $\chi^2 \approx 3360$ values in red. For values of ν_{DC} greater than the threshold at a given S/N the scintillation should be detectable. By extrapolating the threshold relationship we calculate the minimum detectable scintillation bandwidths ν_{min} using the observed burst S/N . Given the assumptions used in this model we round ν_{min} to the nearest order of magnitude.

APPENDIX B: DERIVATION OF EQ. 3

As per Narayan (1992) the modulation index of an extended source is given by

$$m = \frac{\theta_{\text{diff}}}{\theta_S} \quad (\text{B1})$$

where θ_{diff} is the angle subtended by the diffractive scale r_{diff}/D_d , and θ_S is the apparent angle of the source. In the case where light scattered by an extragalactic screen into an angle $\theta_{\text{scatt},x}$ is incident upon a Galactic screen characterised by $r_{\text{diff},g}$, the modulation index of scintillation from the Galactic screen (m_g) will be given by

$$m_g = \frac{r_{\text{diff},g}}{D_{d,g}\theta_{\text{scatt},x}} \quad (\text{B2})$$

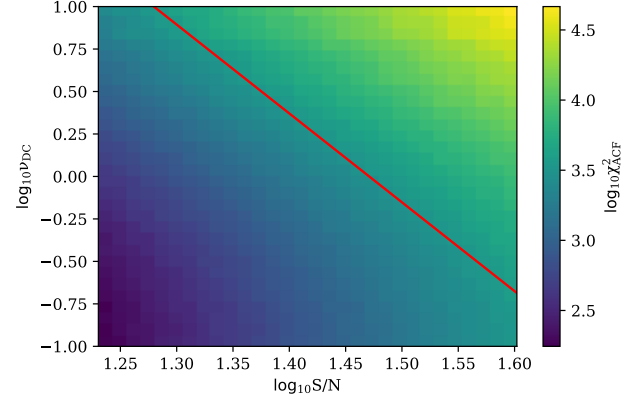


Figure A1. $\log_{10} \chi^2$ values for the significance of scintillation structure in the burst ACF as a function of burst S/N and ν_{DC} . Red line represents the detection threshold, fit to χ^2 values of ≈ 3360 , where the CDF of the χ^2 distribution is ≈ 0.5 .

where $D_{d,g}$ is the distance to the Galactic screen from the observer. The diffractive scale the Galactic screen may also be approximated as $r_{\text{diff},g} \sim \lambda/2\pi\theta_{\text{scatt},g}$ (Narayan 1992), yielding

$$m_g = \frac{\lambda}{2\pi\theta_{\text{scatt},g}\theta_{\text{scatt},x}D_{d,g}} \quad (\text{B3})$$

where λ is the observed wavelength. As per Macquart & Koay (2013) scattering angles can be expressed as scattering times following $t_{\text{scatt}} = D_d D_s \theta_{\text{scatt}}^2 / [c D_{ds}(1+z_d)]$, where z_d is the redshift at the screen. Substituting the scattering angles for scattering times gives

$$t_{\text{scatt},g} t_{\text{scatt},x} = \frac{1}{(2\pi\nu)^2 m_g^2 (1+z_x)} \frac{D_{s,x} D_{d,x}}{D_{ds,x}} \frac{D_{s,g}}{D_{ds,g} D_{d,g}} \quad (\text{B4})$$

When $m_g = 1$, the left hand side becomes \leq the right hand side, and the general form of Eq. 2 is recovered. By assuming that the screens are close to their respective ends of the path length (i.e. they are associated with the Milky Way and host galaxies), we can approximate $D_{d,x} \approx D_{ds,g}$, and $D_{s,x} \approx D_{s,g} \approx D_s$, reducing the above expression to

$$t_{\text{scatt},g} t_{\text{scatt},x} \approx \frac{D_s^2}{(2\pi\nu)^2 m_g^2} \frac{1}{D_{d,g} D_{ds,x}} \quad (\text{B5})$$

Exchanging $t_{\text{scatt},g}$ for $1/2\pi\nu_{\text{DC}}$ via Eq. 1 and recognising that $D_{d,g}$ and $D_{ds,x}$ are L_g and L_x respectively yields Eq. 4

$$L_x L_g \approx \frac{D_s^2}{2\pi\nu^2 (1+z_x)} \frac{\nu_{\text{DC}}}{t_{\text{scatt}}} \quad (\text{B6})$$

APPENDIX C: ANISOTROPIC SCATTERING SCREENS

The constraints on the $L_x L_g$ product are derived from the condition, that to have fully modulated diffractive scintillation at the second screen, the coherence length set by the diffractive scale of the first scattering screen ($r_{\text{diff},1}$) must be greater than the scattering angle of the second screen projected back onto that screen (Ocker et al. 2022b), i.e.

$$r_{\text{diff},1} \geq \theta_{\text{scatt},2} D_d. \quad (\text{C1})$$

The implicit assumption within this condition is that the thin screens are two-dimensional and isotropic. Under this assumption the extent of angular broadening caused by the first screen is equivalent to the extent of the source as seen by the second screen. If however, the screens were anisotropic, the direction of angular broadening will also be important. In the extreme case where each screen is one dimensional, e.g. scattering by a filament or tidal stream similar to that observed by Wang et al. (2021), then the angular extent of the source seen by the second screen will be given by the projection of the image scattered by the first screen onto the second. The condition to observe fully modulated diffractive scintillation at the second screen then becomes

$$r_{\text{diff},1} \geq \theta_{\text{scatt},2} D_d \cos \phi, \quad (\text{C2})$$

where ϕ would be the angle between the one-dimensional screens if they were projected onto a plane perpendicular to the optic axis.

For parallel, one-dimensional screens the constraints will remain unchanged. Conversely, for perfectly orthogonal screens, the second screen will always observe the source to be point-like, regardless of the extent of angular broadening from the first screen. In this case, the scattering in each dimension will be completely independent and we will be unable to constrain the scattering geometry. Constraints on the two-screen distance product are therefore completely degenerate with the anisotropy of the scattering screens.

We highlight, however, that in the case of anisotropic scattering screens, it is expected that the shapes of both the temporal impulse response function (i.e. the temporal broadening profile) and the spectral ACF of the scattered pulse will differ from those used here. Specifically, in the case of the temporal impulse response function, anisotropic screens are expected to show a greater fraction of intensity at larger time delays (Cordes & Lazio 2001; Rickett 2006). The more one-dimensional these screens become, the greater the difference in expected pulse morphology will be. Within our sample, the observed pulses are well described by the pulse morphology expected for scattering through an isotropic, two-dimensional thin screen, particularly FRB 20210320C. We, therefore, conclude that significant anisotropy in the scattering screens associated with our observations is unlikely, and we leave a rigorous treatment of the expected FRB morphology for scattering through anisotropic screens to a future work.

APPENDIX D: ADDITIONAL FIGURES

This paper has been typeset from a $\text{\TeX}/\text{\LaTeX}$ file prepared by the author.

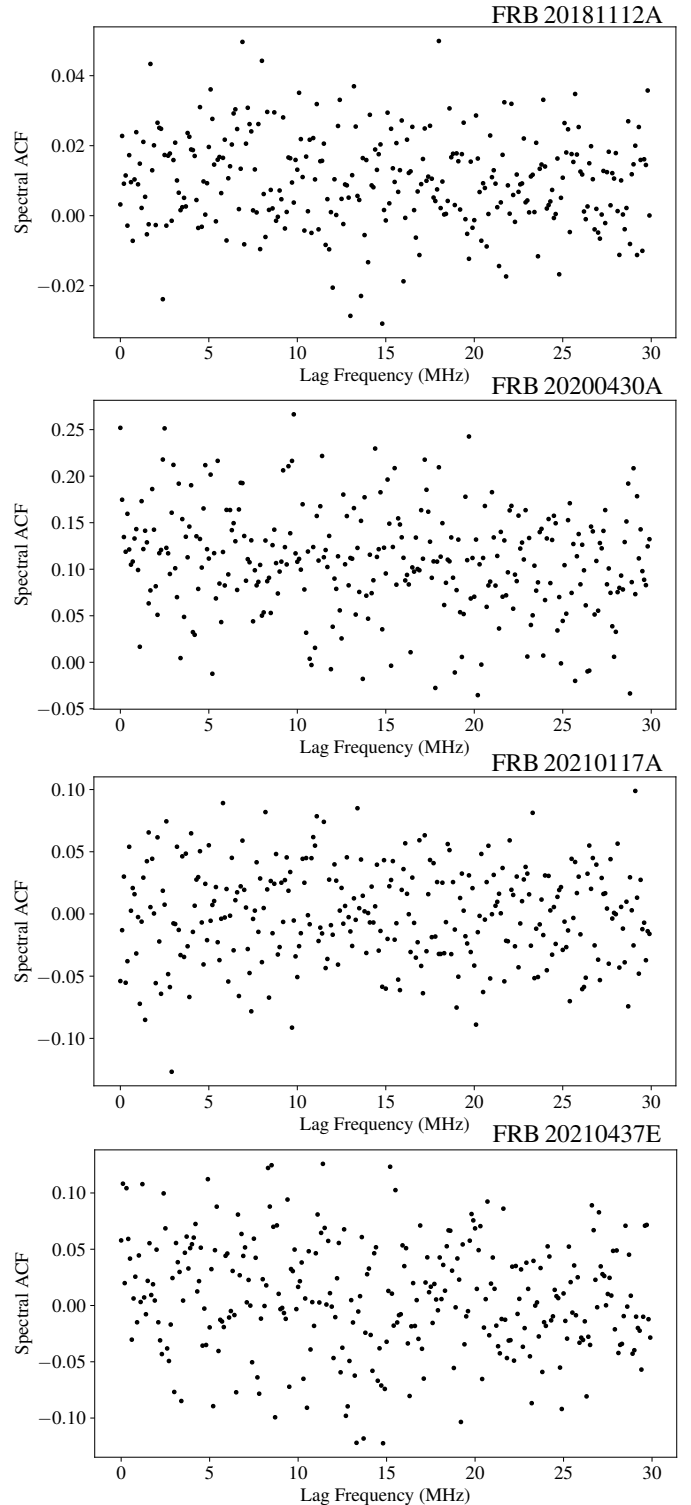


Figure D1. Time-integrated spectral ACFs for FRBs within the sample confirmed not to scintillate. Each panel is labelled with the relevant FRB name.

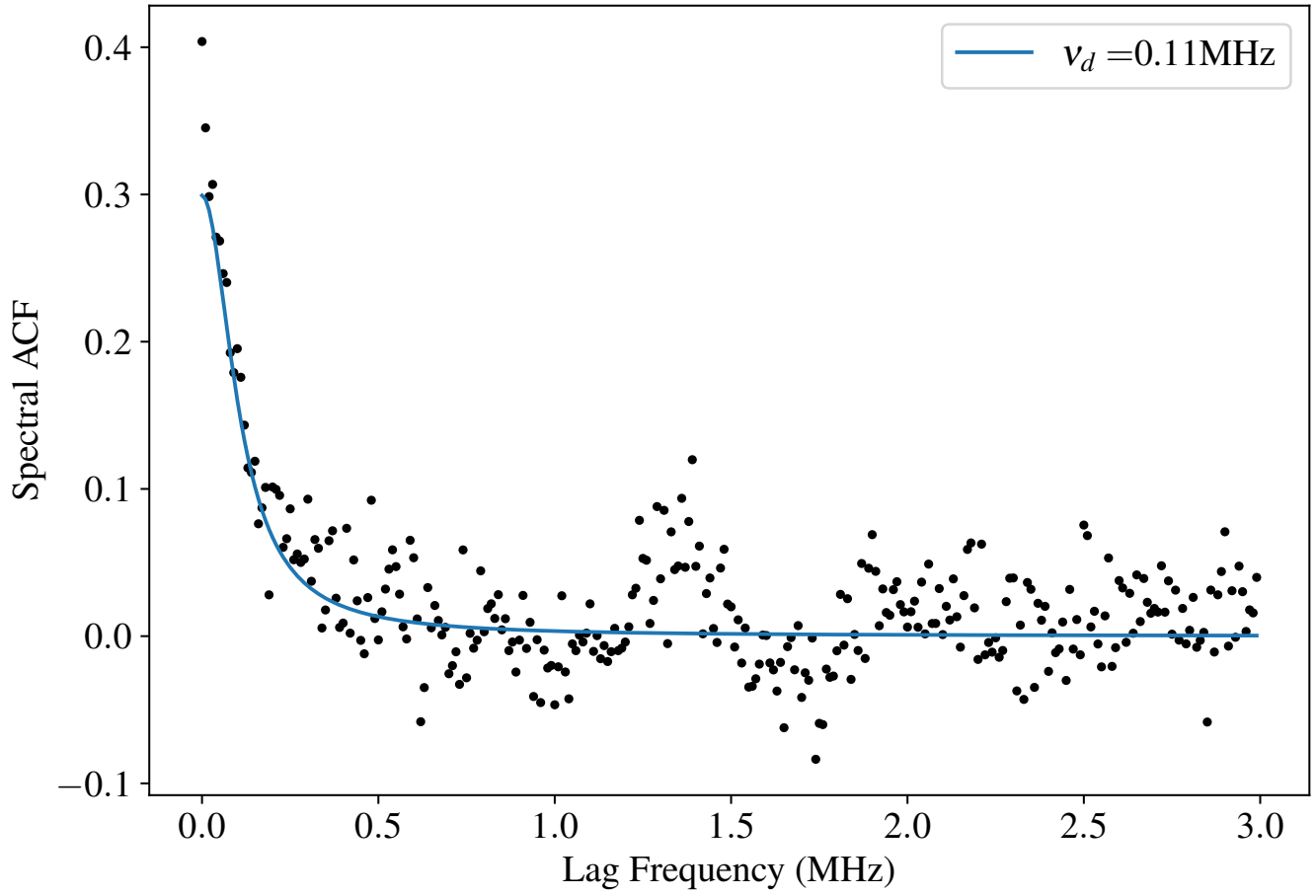


Figure D2. Time-integrated spectral ACF for FRB 20190711A, for which we found insufficient evidence to prove scintillation.

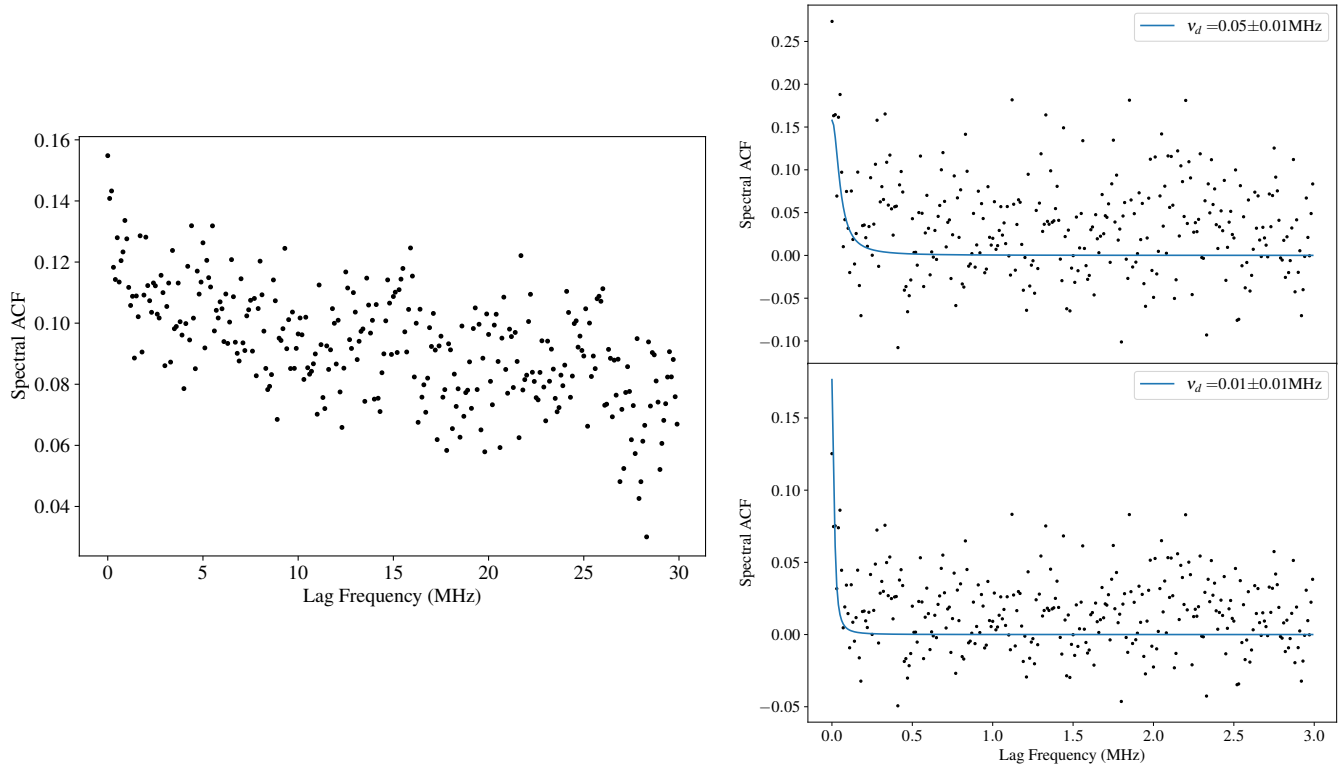


Figure D3. Time-integrated spectral ACFs for FRB 20190102C, for which we found insufficient evidence to prove scintillation. *Left:* ACF over the full used bandwidth. *Right:* ACFs for the *top* and *bottom* sub-bands respectively.

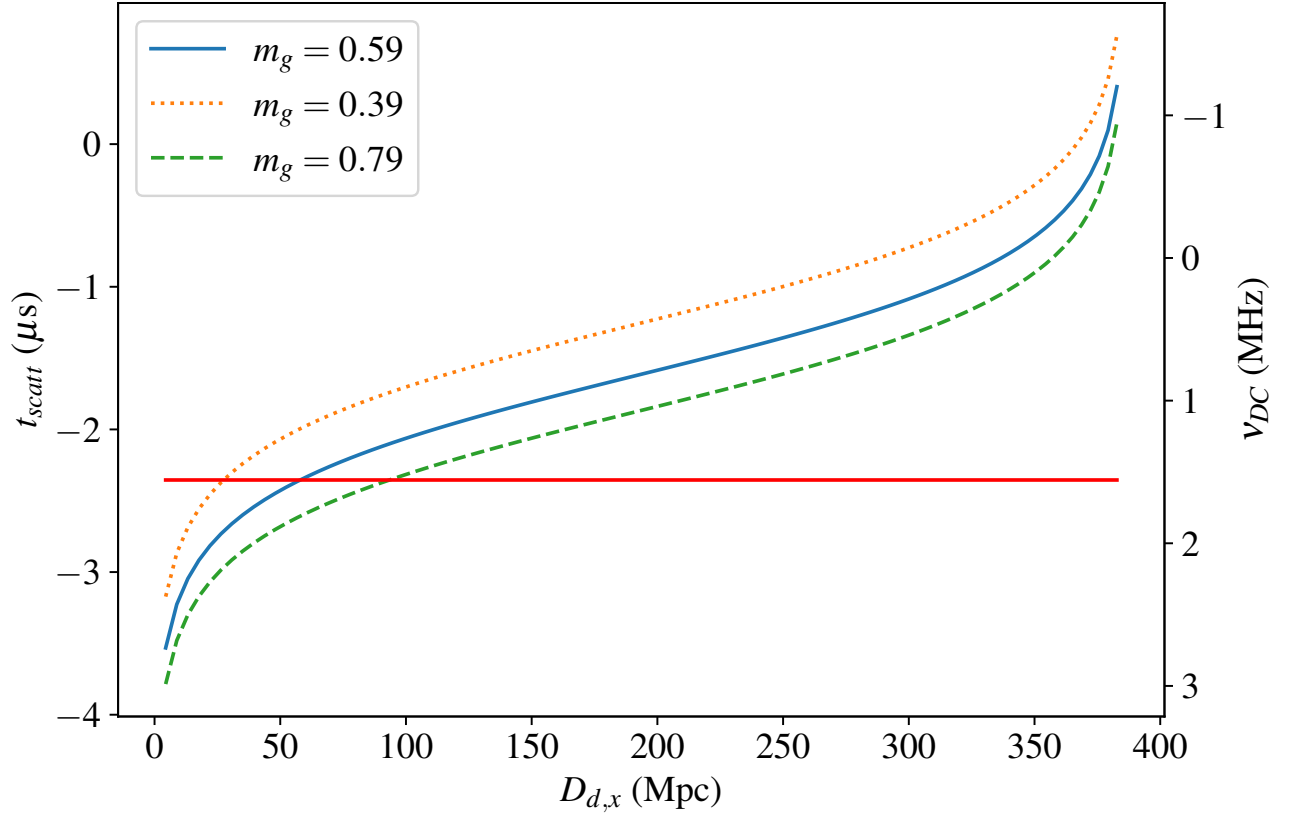


Figure D4. Scattering timescale and corresponding decorrelation bandwidths (assuming $2\pi\nu_{DC}t_{\text{scatt}} = 1$) contributed by a potential third IGM screen which would be responsible for suppressing the modulation of spectral scintillation in FRB 20201124A through angular broadening. The blue line corresponds to the calculation for the measured modulation index of $m_g = 0.59$, additional dotted and dashed lines display how the required scattering time changes with the modulation index. The red line displays the observed bandwidth of FRB 20201124A.

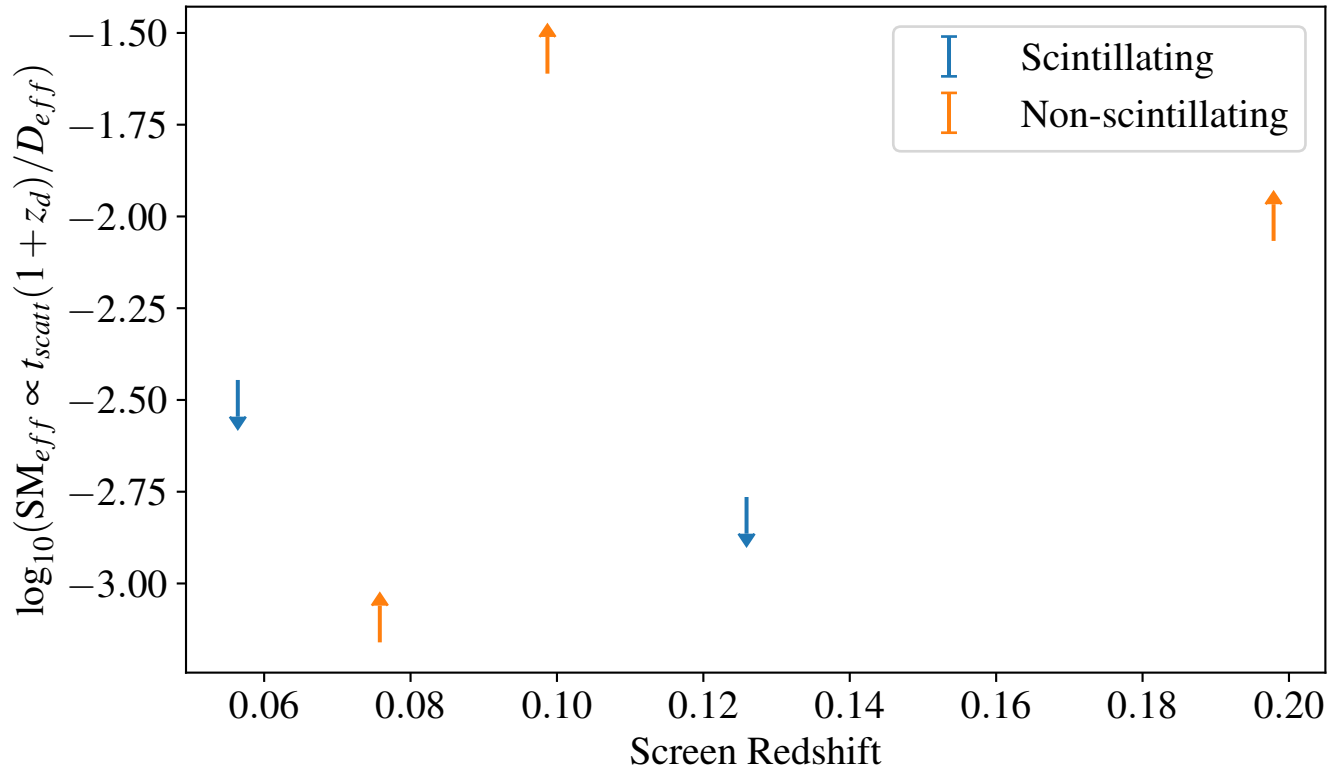


Figure D5. Limits on values proportional to the effective scattering measure defined in [Macquart & Koay \(2013\)](#) from scintillating and non-scintillating FRBs as discussed in §4.1 and 4.2 and §4.5 respectively.